processes

MDPI

Article

Convective Heat Transfer Motivated by Liquid-to-Vapor Density Difference in Centrifugal Force Field of Axially Rotating Loop Thermosyphons

Shyy Woei Chang [1,*], Min-Fu Hsieh [2], Pey-Shey Wu [3] and Wei Ling Cai [1]

[1] Department of Systems and Naval Mechatronic Engineering, National Cheng Kung University, Tainan City 70101, Taiwan; p18071018@mail.ncku.edu.tw
[2] Department of Electrical Engineering, National Cheng Kung University, Tainan City 70101, Taiwan; mfhsieh@mail.ncku.edu.tw
[3] Department of Mechanical and Automation Engineering, Da-Yeh University, Changhua 51591, Taiwan; pswu@mail.dyu.edu.tw
* Correspondence: swchang@mail.ncku.edu.tw

Abstract: The innovative rotating looped thermosyphons (RLTs) with and without a coil insert were proposed with cooling applications in rotating machinery. The spatial gradients of body forces among the vapor–liquid mixture of the distilled water in a strong centrifugal acceleration field motivated the flow circulation in a RLT to facilitate the latent heat transmissions. The effective thermal conductivity (K_{eff}), the thermal resistance (R_{th}), the Nusselt numbers in the condenser (Nu_{con}) and evaporator (Nu_{eva}), and the Nusselt number of the airflow induced by the rotating bend of the condenser ($Nu_{ext,con}$) of each RLT were measured at various rotating speeds and heat powers with two filling ratios of 0.5 and 0.8. The increase of filling ratio from 0.5 to 0.8 to maintain a thin liquid film along the rotating inner leg of each RLT substantially improved the heat transfer performances. The K_{eff}, Nu_{con}, Nu_{eva}, and $Nu_{ext,con}$ were increased with rotating speed, leading to the corresponding reduction of R_{th}. On the basis of the experimental data, the empirical correlations that were used to calculate R_{th}, K_{eff}, Nu_{con}, Nu_{eva}, and $Nu_{ext,con}$ of the RLTs at the two filling ratios with and without coil were proposed to assist the relevant design applications.

Keywords: rotating looped thermosyphon; passive heat transfer; rotating machinery cooling

check for updates

Citation: Chang, S.W.; Hsieh, M.-F.; Wu, P.-S.; Cai, W.L. Convective Heat Transfer Motivated by Liquid-to-Vapor Density Difference in Centrifugal Force Field of Axially Rotating Loop Thermosyphons. *Processes* **2021**, *9*, 1909. https://doi.org/10.3390/pr9111909

Academic Editor: Ireneusz Zbicinski

Received: 29 September 2021
Accepted: 20 October 2021
Published: 26 October 2021

Publisher's Note: MDPI stays neutral with regard to jurisdictional claims in published maps and institutional affiliations.

Copyright: © 2021 by the authors. Licensee MDPI, Basel, Switzerland. This article is an open access article distributed under the terms and conditions of the Creative Commons Attribution (CC BY) license (https://creativecommons.org/licenses/by/4.0/).

1. Introduction

Thermal physics in a rotating heat pipe (RHP) is analogous, to a certain extent, with the free convection motivated by the gradients of fluid density in the earth's gravity. The large vapor-to-liquid density difference in a much stronger centrifugal acceleration field with latent heat transmissions, however, differentiates and promotes the heat transfer mechanisms in a RHP from that with free convective flows. Li and Liu [1] conducted a review to highlight the effects of rotation mode and speed, capillary structure and geometries of condenser and evaporator, heat power, filling ratio, and working fluid on the performances of RHPs. The uniqueness of the thermal flow phenomena in an RHP originated from the particular interfacial segregation of the liquid flowing in the direction of centrifugal force. While the transition to annular flow in a concentric RHP was accelerated by the coil wick that increased the axial fluid velocity, the screen wick suppressed the axial temperature gradient. With an axial RHP rotating at a rated speed, the heat transfer performance was promoted by extending the rotating arm. The improved temperature uniformity from that in a cylindrical RHP was achieved using the tapered and stepped RHPs. The optimum filling ratio for each type of RHP depended on the type of working fluid and the operating condition. The heat transfer rate in the condenser was much higher and close to that in the evaporator for the pool and annular flows in an RHP. With a straight RHP, the thermal resistance was, respectively, increased and decreased

after raising the heat power at low and high rotation speeds [1]. Referring to the relative direction between the axes of an RHP and its rotating vector, the previous works have been characterized into the concentric, radial, and axial RHPs.

1.1. Concentric Rotating Heat Pipe

Lee and Kim [2] studied the flow and heat transfer characteristics in a concentric RHP with a coil insert at different coil helix angles, rotational speeds, and filling ratios. A pumping effect that motivated the axial flow of liquid film was induced by a spiral coil. The pumping effect enhanced the condensation heat transfer rate and extended the transport limit, but was weakened at higher rotational speeds when the flow transited toward the annular flow, within which the pumping effect was diminished. Such a rotational effect became more dominant by increasing the filling ratio. With a larger helix angle, the pumping effect was promoted with an earlier transition to the annular flow in the RHP. Song et al. [3] integrated several empirical correlations to model the thermal performance of high-speed RHPs with centrifugal accelerations up to 10,000 g to examine the thermal impacts of filling ratio, rotational speed, and pipe geometry. The overall heat transfer performance deteriorated by the increasing filling ratio, owing to the thickened film thickness in the condenser. Heat transfer rates increased with rotational speed. The tapered evaporator tended to suppress the overall heat transfer rate of the concentric RHP. Later, Song et al. [4] carried out experiments to explore the heat transfer performance of a concentric tapered RHP with water with the filling ratio between 5% and 30% at the maximum centrifugal acceleration of 170 g at rotational speeds up to 4000 rev/min. The heat transfer rates of the RHPs were increased by raising the rotational speed and/or decreasing the filling ratio. Compared to that in the cylindrical RHP, the tapered condenser significantly raised the heat transfer rate. The free convection of the liquid film in the evaporator of the RHP was an important mechanism for transmitting heat flux at high rotational speeds. In their experiments that measured the thermal resistances and liquid film Nusselt numbers of a non-stepped RHPs at speeds of 2000–4000 rev/min with centrifugal acceleration in the range of 40–180 g, the results indicated natural convection in the liquid layer of the evaporator [5]. The thermal resistance of the evaporator was reduced by increasing the rotational speed and/or the heat flux; this result was less than and similar to that of the condenser in the cylindrical and tapered RHPs, respectively.

Bertossi et al. [6] proposed a steady-state model of heat–mass transfers to highlight the thermal impacts of rotational speed and evaporator wall-to-vapor temperature difference. A procedure to identify the operating conditions for obtaining an optimal filling ratio at a given saturation temperature was formulated. Xie et al. [7] measured the temperature of a concentric stepped RHP and showed the reduced axial temperature gradient in comparison with the solid pipe. Lian et al. [8] developed a numerical model to predict the two-phase flow and heat transfer phenomena in a concentric RHP to examine the thermal impacts of evaporator/condenser heat transfer rate, rotational speed, and filling ratio. The thermal resistance of the RHP was slightly reduced by increasing the evaporator/condenser heat transfer rate. Considerable thermal performance improvements were achieved by increasing the rotational speed due to the associated enhancement of natural convection in evaporator. Chen et al. [9] incorporated a vertical RHP in the abrasive milling tool, with the heat transfer mechanism in the evaporator and condenser simulated at different cooling conditions, filling ratio, and feed speed at the rotational speed of 1600 rev/min. The temperature in the evaporator section of the machine tool was reduced by 65.7% compared to that without RHP. Chatterjee et al. [10] carried out an experimental study to investigate the flow transitions in a partially filled concentric RHP with emphases on the effects of liquid flow rate, pipe inclination, pipe length, and diameter on the flow transitions. The rotational speeds for flow transitions to, and breakdown of, annular flow were reduced by increasing the tilt angle of the RHP. Such flow transition to annular flow emerged at a lower rotational speed in a larger diameter pipe, but was independent of pipe length.

1.2. Radial Rotating Heat Pipe

Ling et al. [11] carried out an analytical study to predict the liquid film distributions in the condenser and the vapor temperature drop along the radial RHP. The diameter, rotational speed, and operating temperature range were the important factors affecting the RHP performance. The heat transfer limitations emerged at the raised heat power and rotational speed, or the decreased RHP diameter. Later, the effects of non-condensable gases on the thermal performance deterioration of the radial RHP were analytically and experimentally studied [12]. The RHP using sodium as the working fluid exhibited high effective thermal conductivity, 60–100 times that of a copper. The experimental results measured from two radial RHPs with different diameters showed heat power as an important parameter [13] that effects the effective heat conductance by altering the condensation temperature. When the cooling airflow rate over the condenser was increased to enlarge the heat transfer capacity of the condenser, the operating temperature of the RHP was reduced and the effective length of the condenser was shortened, leading to the steeper temperature distribution across the condensation length. The RHP with a smaller diameter showed a larger temperature drop along the pipe length than that with a larger diameter at the similar operating conditions.

Waowaew et al. [14] measured and correlated the heat flux transferred by a radial RHP to study the effects of pipe diameter, pipe's length-to-diameter (aspect) ratio, working fluid (R123, ethanol, and water) at the filling ratio of 60%, and rotational speed. The range of RHP inclination angle was 0–90°. The transferred heat flux was decreased by increasing pipe diameter, aspect ratio, and/or density of fluid, while it increased with the centrifugal acceleration. Aboutalebi et al. [15] measured the thermal resistance of a closed loop pulsating radial RHP to examine the effect of rotational speed on its thermal performance at different heat powers and filling ratios (FR) ranging from 0.25–0.75. The thermal resistance was reduced by increasing heat power, and/or rotational speed. When the heat power exceeded the partial dry-out limits, the increase of heat power led to the thermal performance deterioration. At all the rotational speeds tested, the optimum filling ratio was 0.5. Li et al. [16] examined the thermal performances of the radial RHPs with four types of wicks, including grooved (G), sintered (S), sintered–grooved composite (SG), and grooved with half sintered length (SGH), at the weak centrifugal accelerations of 1–2 g. The centrifugal acceleration adversely affected the thermal performance of the RHPs by recessing the liquid in the condenser. Among the capillary structures tested, the RHP with SG wick exhibited the best thermal performance but was noticeably affected by increasing centrifugal acceleration. Later, this research group [17] incorporated a radial RHP into a grinding wheel to enhance heat dissipation of the contact zone during a machining process. The simulation result revealed the natural convection in the evaporator and film condensation within the radial RHP. In contrast with the higher temperature of about 750 °C and the grain refinement in the absence of RHP cooling, the lower temperatures with good surface morphology were achieved by installing the RHPs.

Chang and Cai [18] examined the flow structures of vapor–liquid circulations, boiling, and condensation heat transfer rates, as well as overall thermal resistances, of a radially rotating two-phase loop thermosyphon thin pad. After raising the centrifugal acceleration from 0 to 1.1 g, the churn flow boiling structure transited to intermittent boiling flow structures with the temporal drifts of vapor bubbles along the vortical orbits. Further increasing the centrifugal acceleration yielded the boiling flow to the swaying bubbles and then to stable continuous tiny-bubble streams. The heat transfer rates over the evaporator and condenser of the rotating pad increased along with centrifugal acceleration. The thermal resistance was decreased by increasing heating power and/or centrifugal acceleration. On-ai et al. [19] experimentally studied the effects of centrifugal acceleration and heating power on the thermal performance of a radially rotating closed-loop pulsating heat pipe. After raising the centrifugal acceleration or heating power, the amplitude (frequency) of the oscillatory temperature variation was reduced (increased), and the circulation rate was increased to reduce the thermal resistance. Liou et al. [20] studied the thermal performances

of a radially rotating pulsating heat pipe configured as interconnected channels in a thin pad with a 50% filling ratio of water. After raising the centrifugal acceleration from 0 to 27.8 g, the intermittent vapor slugs transited toward tiny bubbly flow to, respectively, weaken and enhance the heat transfers over the evaporator and condenser. The overall thermal resistance accordingly decreased along with the centrifugal acceleration to reflect the competing heat transfer responses in the evaporator and the condenser of the RHP [20].

1.3. Axial Rotating Heat Pipe

Faghri et al. [21] simulated the vapor flow in an axial RHP at rotational speeds between 0 and 3800 rev/min to show the considerable effects of rotational speed and radial Reynolds number on the pressure and the axial, radial, and tangential fluid velocities. The axial and tangential shear stress components increased, along with the evaporation rate and the rotational speed. Jankowski et al. [22] experimentally studied the thermal performance of an S-shaped curved heat pipe that rotated axially. An annular gap wick structure in the heat pipe ensured the heat transmission for nonrotating operations. With the circulation of methanol between evaporator and condenser, a highly effective thermal conductivity with the curved RHP at the centrifugal acceleration about 400 g for heat powers up to 200 W was achieved.

For applications to heating, ventilating, and air conditioning systems, Yau and Foo [23] experimentally studied the thermal performances of the straight and leveled axial RHPs charged with R134a, R22, and R410A to explore the thermal impacts of rotational speed, radial displacement, and refrigerants. The evaporator heat transfer rate was increased with the increase of rotational speed and/or radial displacement. The straight radial RHPs showed the best thermal performances among the comparable group. At similar geometric and operating conditions, the higher temperature gradients in the RHPs with R410A were observed. Hassan and Harmand [24] measured the axial temperature drops, surface Nusselt numbers, and thermal resistances of a radial RHP. The decrease of rotational speed or radius or increase of heat power raised the thermal resistance. The rotating radius did not cause a sensible effect on the maximum surface Nusselt number of the RHP at high heat powers.

1.4. Thermal Management of Electric Machinery

While the diverse effects of rotational speed, filling ratio, and heat power on the thermal performances of the RHPs have been reported in [1–24], the highly effective thermal conductivity of RHPs have been affirmed. To meet global goals to overcome climate change, electrically powered trains driven by sustainable energy sources are replacing heat engines that convert thermal power of fossil fuels into work. The cooling methods for an electric motor with high power density play a crucial role in efficient operations. Gundabattini et al. [25] reviewed the advanced cooling methods with applications to the permanent magnet synchronous motors, including air, water, oil, heat-pipe, and potting silicon gelatin cooling, as well as the cooling schemes utilizing microchannels. In the search for augmenting densities of power and torque of an electric motor with high efficiency, the highly thermally conductive and electrically insulating polymer materials should be pursued in the next generation of electric machines. Deisenroth and Ohadi [26] focused on the recent progress in thermal management of electric motors with particular emphasis on the applications to aviation propulsion. It was concluded that an effective thermal management system was required to cool the motor and the integrated drive unit, as well as the systems of power electronics and condition monitoring. Canders et al. [27] studied the direct slot cooling method to remove the heat at which it was produced so that the complexity and weight of an electric motor cooling system were reduced. An oil-cooling structure for end winding and the stator core of an electric motor was proposed by Guo and Zhang [28] using lubricating oil to transfer the thermal power generated in the motor. In comparison with the water-cooled motor, the proposed oil-cooling scheme exhibited a lower temperature rise rate with moderate axial material temperature gradients. Fujita et al. [29]

developed the motor stator cooling method using refrigerant and compared the cooling performance with that of conventional water cooling. With the refrigerant cooling, the rated torque was higher than that with water cooling when the electromagnetic structures were similar. Wu et al. [30] developed an electromagnetic-thermal numerical model to implement the thermal management of an interior permanent magnet synchronous electric motor. By taking the effect of the Taylor vortex in the air gap between the stator and rotor into account, the significance of shaft cooling was highlighted for an electric motor. While most previous works for devising cooling schemes in an electric motor, such as [25–29], have focused on the cooling methods integrated with the stationary components, the significance of rotor cooling was pointed out in [30]. As a new passive and effective practical measure to axially transfer the heat flux generated in the rotor core into the air plenums at the two axial ends of the rotor in an electric motor, the axially rotating looped thermosyphon (RLT) is proposed as a conductor with augmented thermal conductivity from the RLT wall. Figure 1 shows the configuration of the electric motor fitted with the RLT as a passive rotor cooling device. A stream of cooling airflow over the outer surface of each exposed RLT (condenser section) is induced by the surrounding wind shear to transfer the condensation and latent heat into the air plenum that is entrapped under the extended cylindrical cooling jacket. The convective heat transfer rate of the Couette-type flow in the air plenum chamber is further boosted by the agitating effect of the rotating bend of the exposed RLT (condenser) section. Inside the RLT, the condensate in the condenser section is driven radially outward by the centrifugal acceleration to facilitate the vapor–liquid circulation in the loop. Along with the vapor–liquid circulation driven by the liquid-to-vapor density difference in the centrifugal force field, the heat flux generated in the rotor core is axially transferred toward the air plenum chamber in an electric motor. The required thermal power to facilitate the boiling activities in an RLT is transferred from the hot rotor, not additionally supplied. Nevertheless, the windage loss of the rotor in an electric motor is increased when the condenser bend of the RLT spins with the rotor.

To enhance the applicability of the test results, the difference between the present and previous works [1–24] in the context of the research methodology is the adopted approach for increasing the centrifugal acceleration by extending the rotating radius to about 4–16 times of the rotor radius in a small or medium electric motor. With a similar centrifugal acceleration, the rotating speed of the present test rig can be reduced to 2–4 times the rotor speed of an emulated electric motor. At the limited test speed in the laboratory, the increase of the rotating radius can considerably extend the test range of centrifugal acceleration to map the larger speed range of an electrical motor with a smaller rotor radius. By installing the RLTs in a rotor of an electric motor with a high power density, the thermal power generated in the magnets can be transferred out of the lumped rotating assembly into the air chambers entrapped at the two axial ends of the rotor without consuming the additional cooling power. Together with the augmented heat transfer rate surrounding the condenser bend of each RLT as a result of rotation, the heat transmissions over the inner surface of the cooling jacket of the stator are also promoted to reduce the rotor and motor temperatures. When occasions require passive heat transmissions out of a rotating assembly with high thermal power density, the present RLTs can be considered as its potential applications. As far as the authors' knowledge, this is the first attempt to utilize the RLT for the axial heat transmission out of the rotor core in an electric motor. Heat transfer studies for such an axially rotating looped thermosyphon with an eccentricity are lacking. The effective thermal conductivities of the RLTs with and without the coil insert, which are correlated into the functions of centrifugal acceleration and heat power for design applications, as well as the effects of rotational speed, heat power, and filling ratio on the effective thermal conductivity, thermal resistance, and the surface Nusselt numbers in the condenser and evaporator of each RLT have been parametrically examined by present study.

In what follows, the experimental facilities, data processing, and experimental program are illustrated in the Experimental Method Section 2. The operating conditions, in terms of evaporator and condenser pressures, as well as the characteristic wall temperature

distribution for each type of RLT are initially presented in the Results and Discussion Section 3. To assist in the interpretation of the thermal physics relevant to the effective thermal conductivity and thermal resistance of the RLT, the Nusselt numbers in relation to the evaporator and condenser of each RLT are subsequently examined. As the external airflow Nusselt number of a rotating condense bend is essential in a practical application of the present RLTs, the Nusselt number results of the airflow surrounding the rotating condenser bend are analyzed. Finally, the results of effective thermal conductivity and overall thermal resistance, which respectively quantify the effective heat transfer rate and the capacity of heat transfer power at a finite heat source-to-sink difference for a RLT, are presented to generate the concluding remarks.

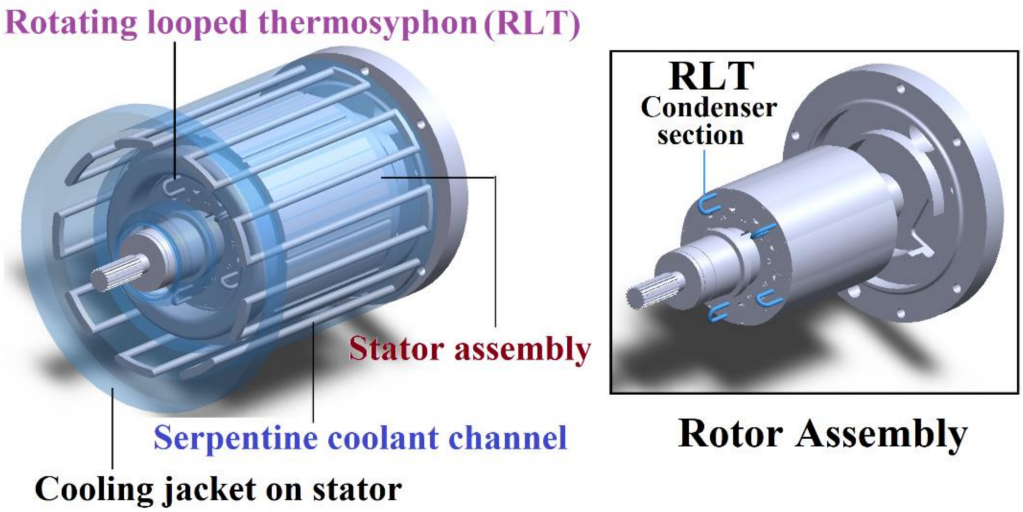


Figure 1. Conceptual cooling design of an electric motor with an RLT in the rotor. The volumetric heat flux in the rotating rotor is transferred passively by the RLTs from the rotor to the air plenum encapsulated within the cylindrical cooling jacket and the end cover of the motor. Liquid coolant flows along the serpentine cooing channel in the cylindrical jacket extended from the stator to transfer all the thermal power out of the motor.

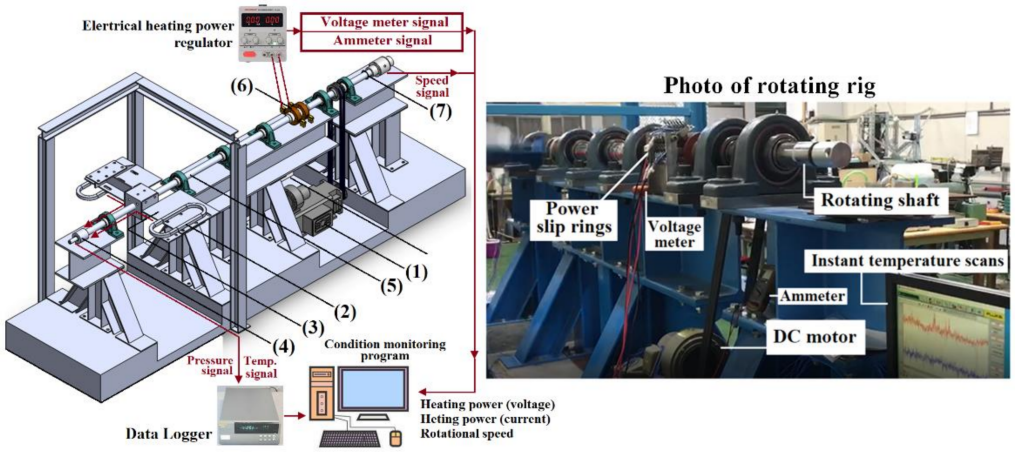
2. Experimental Method

2.1. Experimental Facilities

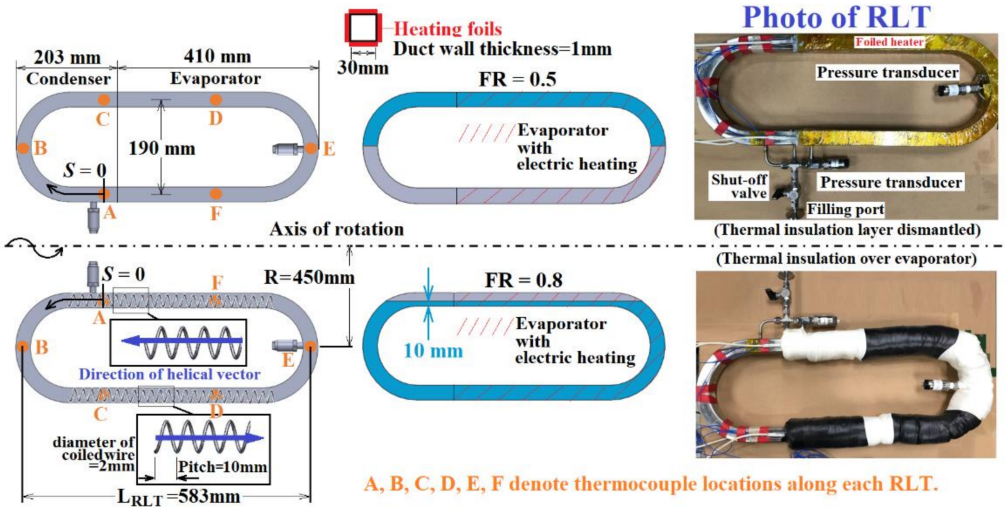
Figure 2a depicts the schematics of the rotating test rig that is driven by a 15,000 W DC electric motor (1). The length, width, and height of the rotating rig are 4.4 m, 1.2 m, and 2.3 m, respectively. The radially rotating looped thermosyphons (RLTs) (2) are installed on the two rotor platforms (3) with the eccentricity (R) of 450 mm. With the extended eccentricity from the typical range of an electric motor, the centrifugal acceleration of a cooling component in a rotor of an electric motor can be simulated by the rotating rig at a reduced rotor speed. A 36-channel instrumentation slip ring (4) is installed at the axial end of the shaft (5) to transmit the signals of thermocouples and pressure transducers to the computer via the Fluke NetDAQ data logger. An online condition monitoring program is installed in the computer to scan the measured RLT temperatures and pressures at each rotating test condition. To feed the electrical heating power to the evaporator section of each RLT, the adjustable electric power supply unit is connected with the power slip-ring unit (6), through which the electric cables are connected in series between the heating foils and the adjustable DC power supply. The rotor speed is detected from the optical detector marked on the shaft (7).

In Figure 2a, the schematic of the instruments measuring the temperatures and pressures of RLTs, as well as the heating powers and rotational speed, is included. The signals of temperatures and pressures of the RLTs are transferred to the data logger via the instrumental slip ring (4). As indicated in the photo of the rotating rig, the instant scans of wall temperature and pressure of the RLTs are permissible using the Fluke data acquisition

program. The voltage and current of heater power fed by the electric power regulator, as well as the rotational speed, are manually input for subsequent data processing.



(a)



(b)

Figure 2. (**a**) Rotating test rig. (1) DC electric motor, (2) RLT, (3) rotor arm, (4) instrumentation slip ring, (5) shaft, (6) power slip ring, (7) optical rotor speed detector; (**b**) RLTs with and without a coil insert at FR = 0.5 and 0.8. The locations of thermocouples A–F along each RLT and pressure sensors are indicated. With FR = 0.8, there is a 10 mm liquid height in the inner leg of each loop prior to the heating process.

Figure 2b shows the RLTs with and without coil insert. In Figure 2b(A–F) denote the thermocouple locations for T_w measurements along the RLT. Such notations are similarly adopted for presenting the T_w distributions along the RLTs, as later illustrated. Considering the strength requirement for a cooling element in a rotating machine, the RLT is made of a 1 mm thick square-sectioned stainless steel duct with an inner height (width) of 30 mm, which is selected as the characteristic length (d) for defining the non-dimensional parameters. The coil made of a 2 mm diameter (d_c) stainless steel wire with a helical pitch of 10 mm, giving the ratio of d_c/d as 0.07, is fitted in each of the two straight legs of the RLT. The orientation of the helical vector for the coil in each straight leg of the RLT is aligned with the direction of the vapor–liquid circulation in the RLT.

The axial spans of the evaporator and condenser are 410 mm and 203 mm, respectively. As indicated in Figure 2b, the nominal length (L_{RLT}) and centerline width of the looped thermosyphon are 583 and 190 mm, respectively. The radii of curvature for each of the two

180° bends at the condenser and evaporator sections are identical, at 80 mm. In Figure 2b, the origin of the loop-wise S coordinate system is positioned at the interface between evaporator and condenser of the inner leg. On the rotating platform, all the outer surfaces of the condenser are exposed in the airflow induced by rotation at the ambient temperature. The direction of the S coordinate follows the circulation direction of the working fluid in each RLT. On the flat endwall of each RLT, there are six foil-type thermocouples installed at the locations A–F along the S-wise centerline to measure the wall temperatures (T_w) along the evaporator and condenser, as indicated in Figure 2b. The distance between the thermocouple and the inner wall of the RLT is 0.5 mm. To emulate the basically uniform flux heating condition, the four evaporator walls are heated by the flexible foil-type electrical heaters with the widths and lengths matching the outer surfaces of the evaporator. The electrical resistance per unit length of each electrical heater is identical. As described previously, these heaters are electrically connected in series to ensure the constant electric current through each heater. The supplied heat flux is determined from the measured heating power and the total heating area of the evaporator. To eliminate air gaps between the evaporator and heater, a thin layer of thermal paste is applied as an interface. As shown by the photos in Figure 2b, the entire evaporator section with the thermocouples and the heating foils is wrapped by a 30 mm thick thermal insulation fiber to minimize the external heat loss. A 10 mm × 10 mm thermal insulation layer with a thickness of 2 mm covers each foil-type thermocouple on the condenser to minimize the effect of airflow on the T_w measurement.

The piezo-metric-type pressure transducers with a precision of 10 Pa are, respectively, installed at the radially inward leg of the condenser and the central of evaporator bend to detect the pressures of condenser and evaporator. As shown by the RLT photo in Figure 2b, the vacuum/filling port and a shut-off valve are connected with the condenser pressure transducer via a T-joint. Prior to installation of each RLT on the rotating rig, the RLT is vacuumed to the absolute pressure of 7.13 Nm^{-2}, which is followed by charging the degassed and distilled water with the volumetric filling ratio of 0.5 or 0.8. The saturation temperatures corresponding to the measured condenser and evaporator pressures are selected as the referenced fluid temperatures to evaluate the Nusselt numbers in the condenser and evaporator. Without heating, at the filling ratio of 0.8, a 10 mm thick liquid film is attached on the inner sidewall of the RLT, as shown by Figure 2a. This layer of liquid film ensures the boiling activities with latent heat transmission at a saturated condition along the inner leg of the evaporator, which considerably improves the heat transfer performance of the RLT, as later demonstrated.

2.2. Data Processing and Experimental Program

The geometrical and heating/cooling configurations of the RLTs with distilled water as the working fluid at the filling ratios of 0.5 or 0.8, with and without the coil insert, predefine the boundary conditions (BC) for each RLT. The effective thermal conductivity (k_{eff}), thermal resistance (r_{th}), and the average heat transfer rates over the evaporator (h_{eva}) and condenser (h_{con}) inside the RLT are governed by heating power, centrifugal acceleration, and the cooling condition over the condenser, which is determined by the forced heat convection of the airflow surrounding the rotating thermosyphon bend and the airflow temperature. With the room temperature of the test rig controlled at 25 °C using the central air conditioning system, the heat transfer rate of the airflow is relevant to the geometric characteristics of the condenser bend, the angular velocity, and the rotating radius of the RLT. Based on the results in [1–24], the functional structures of effective thermal conductivity (K_{eff}), thermal resistance (R_{th}), and averaged Nusselt numbers of the evaporator (Nu_{eva}) and condenser (Nu_{con}) in each RLT follow the general dimensionless form of Equation (1):

$$K_{eff}, R_{th}, Nu_{eva}, Nu_{con} = \Psi\{Ca, Q*, BC\} \quad (1)$$

where K_{eff}, R_{th}, Nu_{eva}, and Nu_{con} are defined as:

$$K_{eff} = k_{eff}/k_w \tag{2}$$

$$R_{th} = r_{th}/\left(k_f d\right) = [(\overline{T_w}_{eva} - T_{amb})/Q]/\left(k_f d\right) \tag{3}$$

$$Nu_{eva} = h_{eva} d/k_f = [q_{eva}/(\overline{T_w}_{eva} - T_{sat,eva})]d/k_f \tag{4}$$

$$Nu_{con} = h_{con} d/k_f = [q_{con}/(T_{sat,con} - \overline{T_w}_{con})]d/k_f \tag{5}$$

In Equations (2)–(5), k_w is the thermal conductivity of stainless steel (RLT wall) of 15 $Wm^{-1}K^{-1}$; Q and q stand for the net convective heat power and heat flux transferred by the RLT. In this respect, the heat fluxes of the evaporator (q_{eva}) and condenser (q_{con}) are defined by the total heat transfer areas of the evaporator and the condenser. $\overline{T_w}_{\mathrm{eva}}$ and $\overline{T_w}_{\mathrm{con}}$ are the wall temperatures averaged from the corrected thermocouple readings from the measurement spot to the fluid–wall interface using one-dimensional Fourier conduction law at the heat flux q. The thermal resistance of RLT (r_{th}) is evaluated from the temperature difference between $T_{w,eva}$ and ambient temperature (T_{amb}). The referenced fluid temperatures for evaluating the Nusselt numbers of the evaporator (Nu_{eva}) and the condenser (Nu_{con}) are the saturated temperatures in the evaporator ($T_{sat,eva}$) and the condenser ($T_{sat,con}$), which are indicated by the table values at the measured evaporator and condenser pressures. The liquid thermal conductivity (k_f) in Equation (3) is calculated from the averaged $T_{sat,eva}$ and $T_{sat,con}$.

The dimensionless centrifugal acceleration (Ca) and heat power (Q^*) are defined by Equations (6) and (7), respectively, as:

$$Ca = \Omega^2 R/g \tag{6}$$

$$Q* = (Qd)/\left(\mu_f h_{fg}\right) \tag{7}$$

In Equation (6), Ω, R, and g, respectively, stand for the angular velocity of RLT, the eccentricity between the centerlines of RLT, and the rotating shaft and gravitational acceleration. The liquid dynamic viscosity (μ_f) and the latent heat (h_{fg}) are evaluated at the averaged saturated temperature and pressure of the RLT. In a steady-state condition, the heat flux transferred by the working fluid out of the condenser (q_{con}) is balanced with the convective heat flux transferred by the airflow at the air temperature of T_{amb}. Based on the temperature difference between the external wall of the condenser and the airflow, the average Nusselt number of the airflow over the rotating condenser bend of the RLT ($Nu_{ext,con}$) is also measured using Equation (8) as:

$$Nu_{ext,con} = [q_{con}/(\overline{T_w}_{ext,con} - T_{amb})]d/k_{air} \tag{8}$$

In Equation (8), $\overline{T_w}_{\mathrm{ext,con}}$ and T_{amb} are the averaged wall temperature measured from the outer surface of the condenser and the ambient temperature of the airflow respectively. The thermal conductivity of air (k_{air}) is calculated at the measured T_{amb}. The governing flow parameter for $Nu_{ext,con}$ is the rotating Reynolds number (Re_Ω) defined by Equation (9).

$$Re_\Omega = \Omega R^2/\nu \tag{9}$$

In Equation (8), the kinematic viscosity of the airflow (ν) is evaluated at the ambient temperature (T_{amb}).

The thermal performance measurements of the two RLTs installed on the two rotor arms of the rotating rig were carried out at the rotating speeds of 100, 200, 300, and 400 rev/min with the corresponding centrifugal accelerations at 4.53, 17.89, 39.63, and 66.62 g. At the rotating speeds tested, five heater powers (Q) in the ranges of 44.42–167.18 W and 152.81–729.47 W for the RLTs with the filling ratios of 0.5 and 0.8 were supplied to alter Q^* at a fixed Ca. The maximum wall temperature in the Q^* range tested was less than 373 K. After regulating Q^* and/or Ca, it generally took 45 min to reach a steady state at which the temperature variations between the several successive T_w scans were less than $\pm$0.3 K.

The net heat transfer power (Q) for calculating the net convective heat flux (q) in Nu_{eva}, Nu_{con}, or $Nu_{ext,con}$ equation is identical. However, the areas selected to define the net convective heat flux (q) for calculating Nu_{eva}, Nu_{con}, and $Nu_{ext,con}$ are the inner surface areas of the evaporator and condenser, and the external area of the condenser bend exposed to the ambience, respectively. The net heat transfer power (Q) for calculating q is determined by subtracting the external heat loss power (Q_{loss}) from the supplied electric heating power. To acquire the heat loss correlation for calculating Q_{loss}, a series of heat loss calibration tests is carried out with the interior of the RLT filled with sand and the exterior of the condenser bend wrapped by the thermal insulation fiber. At each rotating speed of 100, 200, 300, or 400 rev/min, five heating powers are applied to raise the steady-state wall temperatures. It generally takes about 4–8 h to satisfy a steady-state condition during each heat loss test. At each rotating speed, Q_{loss} is proportional to the wall-to-ambient temperature difference with the proportionality increased along with the rotational speed. The Q_{loss} correlation is incorporated with the data processing program for subsequent data reduction. To simulate the temperature field of a rotating machine such as an electric motor, the effective thermal conductivity of the RLT (k_{eff}) is an important "property" that permits the definition of a conduction model for a rotating hot component cooled by the present RLT. The k_{eff} measured follows Equation (10) as:

$$k_{eff} = Q/[(\overline{T_{w}}_{eva} - \overline{T_{w}}_{con}) \times L_{RLT}] \quad (10)$$

In Equation (10), L_{RLT} is the aforementioned nominal length of the RLT, shown in in Figure 2b as 583 mm. $\overline{T_{w}}_{\text{eva}}$ and $\overline{T_{w}}_{\text{con}}$ are the averaged wall temperatures of the evaporator and the condenser.

The experimental uncertainties of Ca, Q^*, Re_{Ω}, K_{eff}, R_{th}, Nu_{eva}, Nu_{con}, and $Nu_{ext,con}$ are estimated following the statistical inference of Kline and McClintock [31]. With the fluid properties indicated by the table values, the main sources attributed to the experimental uncertainties are the measurements of temperature, pressure, rotating speed, and heat power. The fluid properties and latent heat involved in the non-dimensional groups are evaluated from the correlations using T_{sat} or T_{amb} as the determining variable. As the saturation temperatures are correlated into the function of evaporator or condenser pressure in the RLT, the error percentages of T_{sat} and its relevant fluid properties are propagated from the pressure measurements. The precision values, data ranges and the maximum error percentages of the various instruments are summarized in Table 1.

Table 1. Precision values, data ranges, and maximum error percentages of the various instruments for raw data measurement.

Instrument	Precision	Data Range	Max. Error (%)
Voltage meter	0.01 V	32.92–131.25 V	0.03
Ammeter	0.01 A	1.35–5.56 A	0.74
Pressure gauge	0.0001 bar	0.0767–0.7381 bar	0.13
Rotating speed detector	0.1 rpm	100–400 rpm	0.1
Thermocouple	0.3 K	T_{amb} 298–300 K	1.2
		$T_{w,eva}$ 312.8–362.7 K	0.75
		$T_{w,con}$ 313.2–392.8	0.75
		$T_{w,ext.con}$ 311.8–361.6	0.77

As stated in Table 1, with the precision value of 10 Pa for the pressure gauge, the maximum uncertainty of pressure measurements was 0.13% in the data range of 0.0767–0.7381 bar. For the temperature measurements, the experimental uncertainty was 0.3 K, giving the maximum error percentages of T_{amb}, $T_{w,con}$, $T_{w,eva}$, and $T_{w\ ext,con}$ as 1.2%, 0.75%, 0.75%, and 0.77%. The percentage errors for the hydraulic diameter (d) of the RLT duct and the RLT

length (L_{RLT}) caused by the manufacturing tolerance of ±0.1 mm were 0.3% and 0.02%, respectively. With the maximum error percentages for heat power and rotating speed of 1.5% and 1%, the root-mean-square experimental uncertainties at 95% confidence interval for *Ca*, Q^*, Re_Ω, K_{eff}, R_{th}, Nu_{eva}, Nu_{con}, and $Nu_{ext,con}$ were estimated as 1%, 7.42%, 1.56%, 8.9%, 2.58%, 2.92%, 2.01%, and 1.57% respectively.

3. Results and Discussion

3.1. Operating Conditions with Characteristic T_w Distribution of RLT

Prior to the examination of the thermal performances of the RLTs, the variations of the measured RLTs' pressures at the evaporator (P_{eva}) and the condenser (P_{con}) and the corresponding saturated temperatures $T_{sat,eva}$ and $T_{sat,con}$ caused by varying *Ca* (Q^*) at the similar Q^* (*Ca*) for the RLTs with and without coil are exhibited in Figure 3 at (a,c) FR = 0.5 and (b,d) FR = 0.8. In a similar T_w range for the RLTs with and without coil, the Q^* range of Figure 3d with FR = 0.8 was about ten times that with FR = 0.5 for Figure 3c. As the present test procedures limited the maximum T_w for all the RLTs, the extended Q^* range for the RLTs with FR = 0.8 indicted the improved heat transfer performances by converting the superheated heating process in the RLTs with FR = 0.5 to the heating process with saturated vapor at FR = 0.8. In the RLTs with FR = 0.8, the single-phase flow of superheated vapor along the inner leg of the RLT converted the thermal power into the enthalpy increase of the sensible heat, leading to a significant T_w increase at an almost constant specific volume condition, and, hence, an increase in the operating pressures in the evaporator and the condenser. In each plot of Figure 3, the P_{eva} ($T_{sat,eva}$) values were consistently higher than their P_{con} ($T_{sat,con}$) counterparts for all the RLTs with and without coil. Each set of P_{eva} and P_{con} ($T_{sat,eva}$ and $T_{sat,con}$) for the RLTs with the coil at FR = 0.5 and 0.8 were larger than those without coil, owing to the added flow resistances by the coil.

In Figure 3a,b, for the RLTs with and without coil at the FRs of 0.5 and 0.8, the P_{eva} and P_{con} ($T_{sat,eva}$ and $T_{sat,con}$) increased along with *Ca*, owing to the enhanced centrifugal acceleration. In Figure 3a with FR = 0.5, the P_{eva}-to-P_{con} ($T_{sat,eva}$-to-$T_{sat,con}$) differences and the pressure (saturated temperature) differences between the RLTs with and without coil were enlarged when *Ca* increased. However, such enlarged pressure (saturated temperature) differences driven by increasing *Ca* were considerably moderated at FR = 0.8 in Figure 3b. Unlike the RLTs with FR = 0.5, the presence of the liquid phase along the inner and outer legs of the RLTs at FR = 0.8 ensured the heating process along the inner and outer legs at the saturated condition prior to the dry-out limit. With FR = 0.5, the heating process along the inner leg of the RLT took place at the superheated conditions. The substantial thermal performance improvements were, hence, achieved by increasing FR from 0.5 to 0.8 for the RLTs with and without coil, which will be later demonstrated.

In view of the Q^* impact on P_{eva} and P_{con} ($T_{sat,eva}$ and $T_{sat,con}$) for the RLTs with and without coil at FR = 0.5 and 0.8, as typified by Figure 3c,d, all the P_{eva} and P_{con} ($T_{sat,eva}$ and $T_{sat,con}$) were increased by increasing Q^*. For each of the RLTs with FR = 0.5, the saturated vapor was generated in the liquid pool of the outlet leg. Without liquid film in the inner leg of the RLT with FR = 0.5, the heating process along the inner leg of the evaporator transformed the saturated vapor into the superheated state and incurred the considerable pressure and temperature increases along the inner leg of the evaporator that significantly undermined its thermal performances. When the FR was increased from 0.5 to 0.8 to yield the heating process from the superheating to the saturated conditions along the inner leg of the evaporator, the P_{eva}-to-P_{con} differences in each RLT and the pressure differences between the RLTs with and without coil were considerably reduced, as compared by Figure 3c,d. The following thermal performance results subjected to the *Ca* and Q^* impacts were generated under the particular sets of $P_{eva,con}$ and the corresponding $T_{sat\ eva,con}$ at the tested *Ca* and Q^* values for the present RLTs.

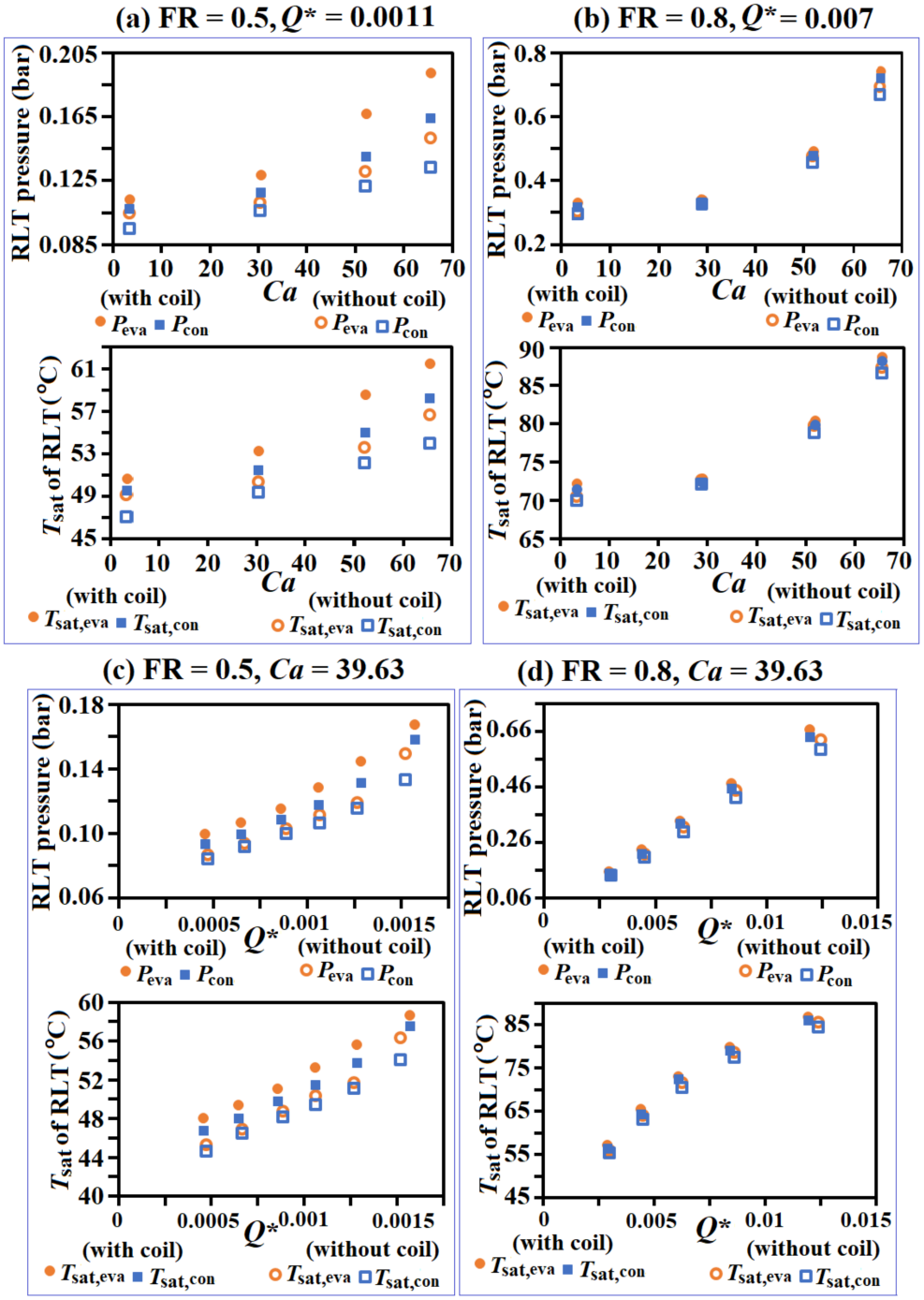


Figure 3. Variations of P_{eva}, P_{con}, $T_{sat,eva}$, and $T_{sat,con}$ against *Ca* (*Q**) at the similar *Q** (*Ca*) values for the RLTs with and without coil at (**a**,**c**) FR = 0.5 and (**b**,**d**) FR = 0.8. All the measured P_{eva}, P_{con}, $T_{sat,eva}$, and $T_{sat,con}$ values increased with *Ca* (*Q**) at a fixed *Q** (*Ca*). The structures of vapor–liquid flow and boiling/condensation processes were influenced by P_{eva} and P_{con}, which were *Ca*- and *Q**-dependent, leading to the consequential *Ca* and *Q** impacts on the thermal performances of the RLTs.

Referring to Figure 2b, which indicates the A to F wall temperature measurement spots along each RLT with or without the coil insert, the regional vapor–liquid phase structures were FR dependent and varied in S-wise direction. In Figure 2b, the liquid–vapor interface in the RLT of FR = 0.5 was formed at the E (B) spots corresponding to the mid-plane of the evaporator (condenser), whereas the liquid–vapor interface was shifted radially outward to the outer leg of the RLT with FR = 0.8. The saturated vapor bubbles in the liquid pool over the D–E span in the evaporator of the RLT with FR = 0.5 were superheated along the

subsequent E–F section. However, the pool boiling region in the evaporator of the RLT with FR = 0.8 was extended from that with FR = 0.5 to cover the entire evaporator bend. Moreover, the subsequent heating process toward location F along the inner leg of the RLT with FR = 0.8 took place at the saturated conditions, with the vapor to be driven radially inward by the segregation force due to the liquid-to-vapor density difference in the strong centrifugal force field. The differential vapor–liquid phase structures from E-to-A section between the RLTs with FR = 0.5 and 0.8 played the dominant role in differentiating their thermal performances, which will be later demonstrated.

Along the inner bend of the condenser from locations A to B in the RLT with FR = 0.5, the condensate was formed from the superheated vapor across the F section and thrown toward the liquid–vapor interface at section B by the centrifugal force. At downstream location A in the RLTs with FR = 0.8, the saturated vapor was condensed along the inner straight leg of the condenser with the sub-cooling length extended from that with FR = 0.5. The differential regional vapor–liquid phase structures in the RLTs with FR = 0.5 and 0.8 generated the different S-wise T_w variations, as typified by Figure 4, in which the loop-wise (S-wise) T_w variations with the high and low Q^* at Ca = 4.53 and 66.62 for the RLTs with and without the coil insert at the filling ratios of (a,b) 0.5 and (c,d) 0.8 are compared. Cross-examining the Q^* between Figure 4a,c, or between Figure 4b,d at Ca = 4.53 or 66.62, the supplied Q^* for the RLTs with the filling ratio of 0.8 were considerably raised from that with FR = 0.5 in the similar T_w range between 293–393 K. This result indicated the hydrothermal consequences of converting the heating process from superheated to saturated vapor. The D-to-E T_w increases along the evaporator loop in the RLTs with FR = 0.5 in Figure 4a,b were substantially higher than those with FR = 0.8 in Figure 4c,d, owing to the different E-to-F heating process at the respective superheated and saturated conditions. Nevertheless, the extended sub-cooling length in the condenser of the RLTs with the filling ratio of 0.8 increased the A-to-C T_w differences from those with FR = 0.5, as compared by Figure 4a,c, and Figure 4c,d.

In the RLT with the filling ratio of 0.5, the presence of the coil insert in the duct without liquid film added the flow resistance along the E-to-F pathway, leading the more evident E-to-F T_w increase compared to that without the coil to impair the thermal performance of the RLT. As compared in Figure 4a or Figure 4b, between the RLTs with and without coil, such impairing effect caused by the coil insert in the RLT with FR = 0.5 was significantly amplified when Q^* was increased. Referring to Figure 3a,c, the raised operating pressure from the added flow resistances of the coil insert in the RLT with FR = 0.5 elevated the corresponding saturated temperatures to incur such enlarged T_w differences at the hottest F spot between the RLTs with and without coil at FR = 0.5, as shown by Figure 4a,b.

By converting the E-to-F heating process from the superheated conditions along the RLTs with FR = 0.5 to the saturated conditions with a liquid film in the RLTs of FR = 0.8, the presence of the spiral coil yielded the S-wise T_w distribution into a wavy-like pattern in Figure 4c,d, especially at the higher Ca and Q^* values. Such wavy-like loop-wise T_w distributions along the RLT with the coil insert at the filling ratio of 0.8 in Figure 4c,d moderately impaired the T_w uniformity but noticeably enlarged the temperature reductions from the T_w values at A and F spots in the RLT without coil. As a result, with a filling ratio of 0.8, the thermal resistance (R_{th}) of the RLT with coil was reduced from that in the RLT without coil, as later demonstrated.

3.2. Nusselt Numbers in Evaporator and Condenser

The Nusselt numbers in the evaporator (Nu_{eva}) and condenser (Nu_{con}) of the RLTs, defined by Equations (4) and (5), are based on the average $\overline{T_{w\mathrm{eva}}}$ and $\overline{T_{w\mathrm{con}}}$ from the S-wise T_w distributions, as typified by Figure 4, which reflect the overall heat transfer performances for the various regions with the different liquid–vapor flow structures along the evaporator and condenser. Figure 5 depicts the variations of Nu_{eva} against Q^* at all the tested Ca values for the RLTs with and without coil at the filling ratios of (a,b) 0.5 and (c,d) 0.8. As compared by Figure 5a,b and Figure 5c,d, the Nu_{eva} level in the RLTs with

FR = 0.8 was significantly raised from that with FR = 0.5 due to the considerable reductions of $\overline{T_{w\text{eva}}}$ attributed from the alleviated T_{weva} variations across the evaporator section seen in Figure 4.

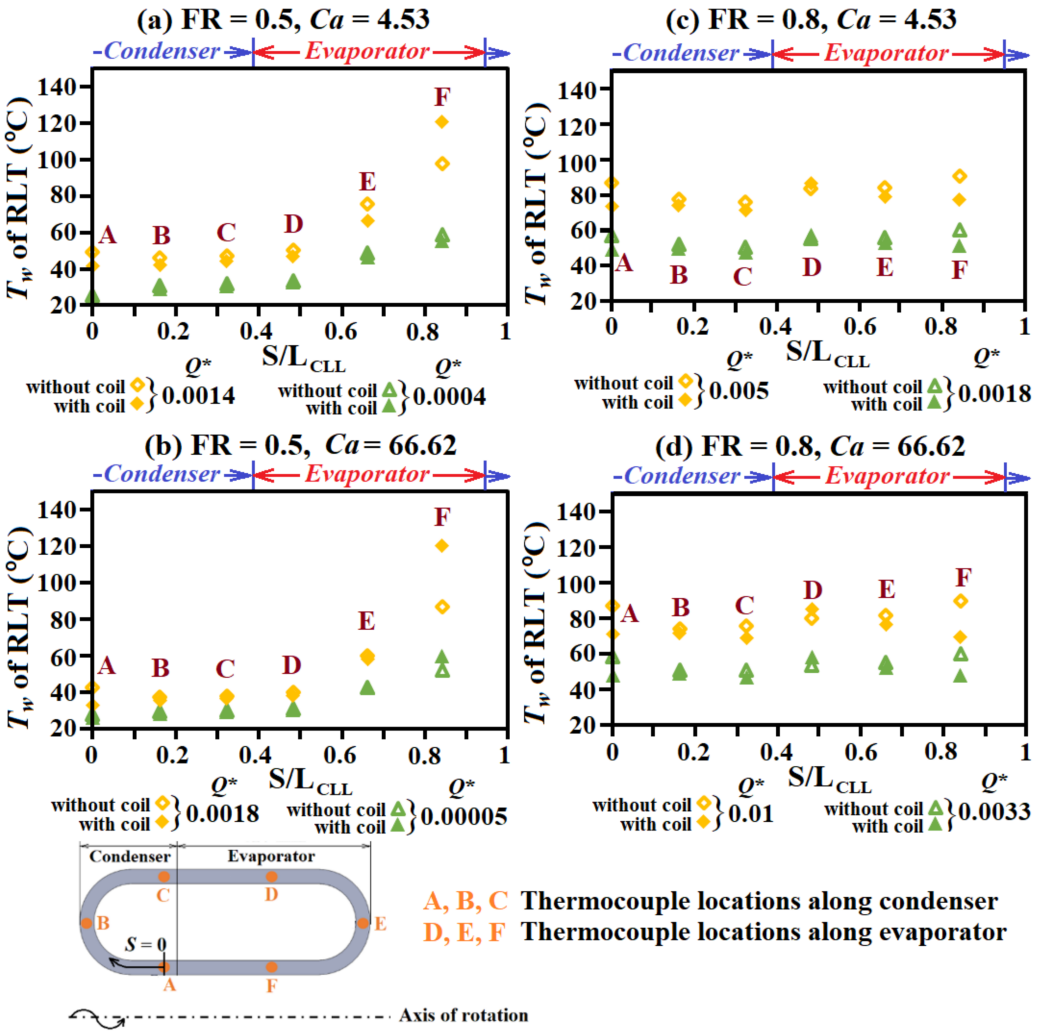


Figure 4. S-wise T_w variations with the high and low Q^* at Ca = 4.53 and 66.62 for the RLTs with and without coil at the filling ratio of (**a**,**b**) 0.5 and (**c**,**d**) 0.8. The high T_w peaks at F locations where the vapor was superheated in the RLTs with FR = 0.5 were diminished in the RLTs with FR = 0.8 by converting the working fluid from superheated to saturated vapor.

As typified by Figure 3, the increase of evaporator or condenser pressure by raising Q^* led to the linear-like $T_{sat,\text{eva}}$ or $T_{sat,\text{con}}$ increase. The varying trends of Nu_{eva} and Nu_{con} against Q^*, hence, depended on the manners of Q^*-driven $\overline{T_{w\text{eva}}}$ and $\overline{T_{w\text{con}}}$ variations. Referring to Equations (4) and (5), the Nu_{eva} and Nu_{con}, respectively, decreased and increased by increasing Q^* when the increasing rates of $\overline{T_{w\text{eva}}}$ and $\overline{T_{w\text{con}}}$ exceeded the Q^*-driven linear increasing rate of $T_{sat,\text{eva}}$ or $T_{sat,\text{con}}$. With the vapor space to be confined by the liquid in each RLT, the heating process along the evaporator was similar to a constant volume process to characterize the pattern of $\overline{T_{w\text{eva}}}$ increase against Q^*. As exemplified by each plot Figure 4, the E-to-F T_w increase was considerably amplified by increasing Q^* so that the increasing rate of $\overline{T_{w\text{eva}}}$ with Q^* exceeded that of $T_{sat,\text{eva}}$. Consequently, the consistent Nu_{eva} decrease with Q^* at a fixed Ca value was seen in each plot of Figure 5.

In the RLT of FR = 0.5 with the coil insert along the outer (inner) leg full of liquid (vapor), the pumping effect generated by the coil, as reported by Lee and Kim [2], was almost diminished. Instead, the coil insert added the drags for vapor–liquid circulation to impede the vapor flow along the evaporator. The Nu_{eva} for the RLT with the coil at FR = 0.5

became lower than that without coil, as compared by Figure 5a,b. With the liquid film attached on the inner sidewall of the inner leg along the RLT of FR = 0.8, the pumping effect of the spring coil was resumed to promote the circulation of working fluid through the evaporator. Unlike the lower Nu_{eva} for the RLT with coil at FR = 0.5, as compared by Figure 5a,b, the Nu_{eva} for the RLT with the coil at FR = 0.8 in Figure 5d turned out to be higher than that in the RLT without coil at FR = 0.8 in Figure 5c, owing to the augmented boiling activities for the E-to-A vapor flow at the saturated condition. Regardless of the heating process at the superheated or the saturated-like condition in the evaporators of the RLTs with FR = 0.5 and 0.8, all the Nu_{eva} data in Figure 5 were increased with *Ca* as the centrifugal force promoted the vapor–liquid circulation.

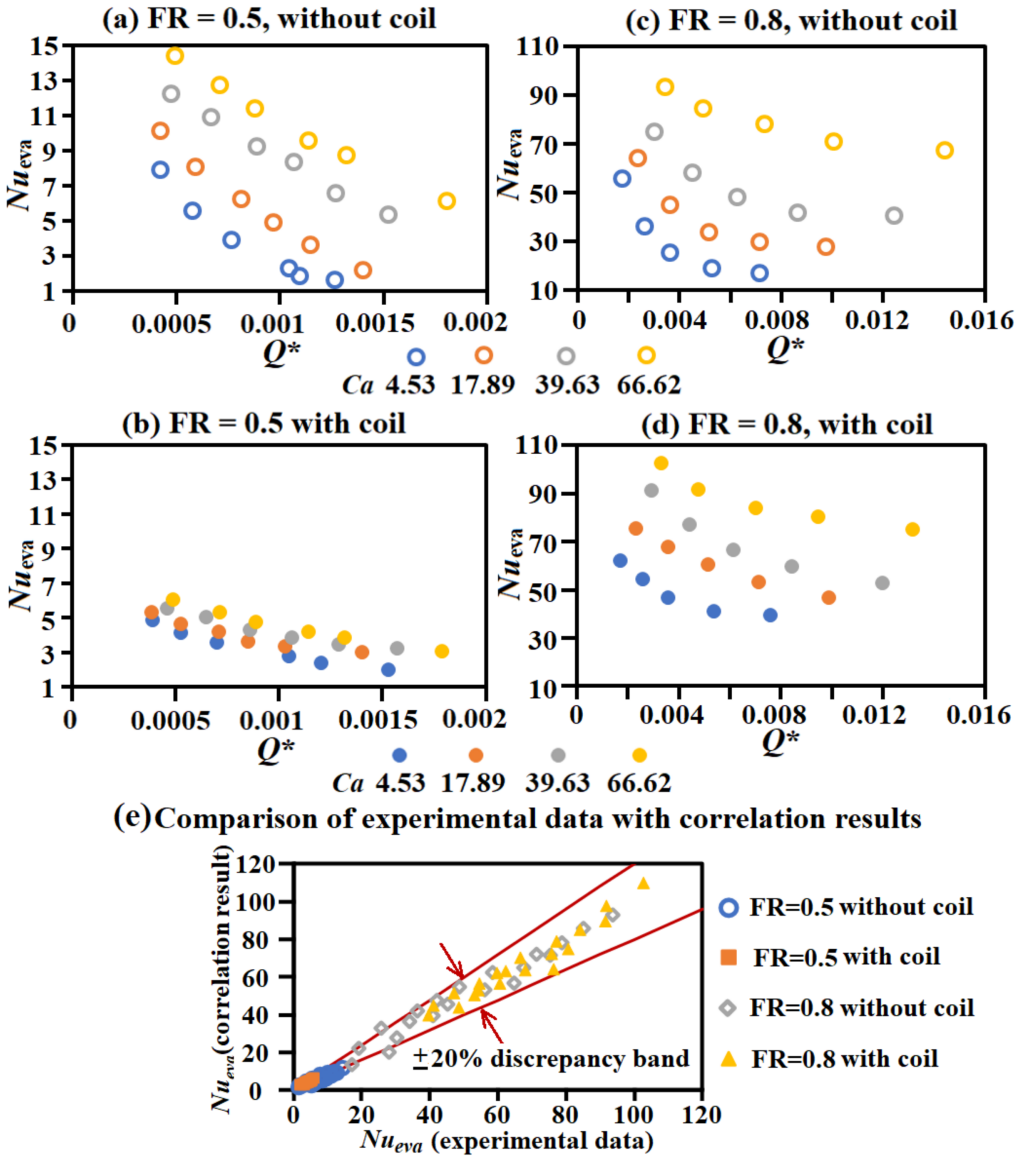


Figure 5. Nu_{eva} variations against Q^* at all the *Ca* values tested for the RLTs with and without coil at the filling ratios of (**a**,**b**) 0.5 and (**c**,**d**) 0.8. (**e**) comparisons of the experimental Nu_{eva} data against the correlation results. All the Nu_{eva} data were decreased with Q^* at a fixed Ca. In Figure 5e, all the results are enveloped by the +20% bound lines.

Following the consistent trend of Nu_{eva} variation with Q^* shown by Figure 5, all the Nu_{eva} data were correlated into equation (11) with the general function of:

$$Nu_{eva} = a\{Ca\} + b\{Ca\}lnQ \quad (11)$$

In Equation (11), the correlative coefficients a and b are functions of Ca. Table 2 summarizes the a and b coefficients for the RLTs with and without coil at FR = 0.5 and 0.8.

The depictions of a and b coefficients against Ca exhibited the consistent trends of linear variations. After identifying the linear functions of Ca for a, b coefficients, the Nu_{eva} correlations of the RLTs with and without coil at FR = 0.5 and 0.8 were generated as Equations (12)–(15) with the maximum discrepancy between the experimental data and correlative results less than ±20%. Such comparative results between the experimental data and the correlation results are affirmed in Figure 5e, where all the results are enveloped by the ±20% difference bound.

$$Nu_{eva} = -37.41 + 0.0653Ca + (-5.76 - 0.0087Ca) \times lnQ \quad \text{FR} = 0.5 \text{ without coil} \tag{12}$$

$$Nu_{eva} = -8.32 - 0.045Ca + (-1.63 - 0.01Ca) \times lnQ \quad \text{FR} = 0.5 \text{ with coil} \tag{13}$$

$$Nu_{eva} = -131.28 + 1.71Ca + (-28.37 + 0.1354Ca) \times lnQ \quad \text{FR} = 0.8 \text{ without coil} \tag{14}$$

$$Nu_{eva} = -34.59 - 0.68Ca + (-14.54 - 0.28Ca) \times lnQ \quad \text{FR} = 0.8 \text{ with coil} \tag{15}$$

Table 2. a and b coefficients in Nu_{eva} correlations for the RLTs with and without coil at FR = 0.5 and 0.8. The a, b coefficients were subsequently correlated into the functions of Ca for devising Nu_{eva} correlation.

Ca	FR = 0.5				FR = 0.8			
	Without Coil		With Coil		Without Coil		With Coil	
	a	***b***	***a***	***b***	***a***	***b***	***a***	***b***
4.53	−5.81	−37.53	−1.67	−8.59	−27.22	−122.33	−15.82	−39.99
17.89	−5.9	−36.03	−1.86	−9.34	−25.6	−95.5	−19.32	−41.45
39.63	−6.12	−34.07	−1.98	−9.63	−24.69	−72.67	−26.8	−67.16
66.62	−6.34	−33.49	−2.33	−11.61	−18.31	−11.62	−33	−78.08

Figure 6 shows the variations of Nu_{con} against Q^* at all the tested Ca values for the RLTs with and without coil at the filling ratios of (a,b) 0.5 and (c,d) 0.8. For the clear depiction of the Nu_{con} results, the data ranges selected to construct Figure 6a–d were different. The variation of Nu_{con} with Q^* reflected the different increasing rates between $\overline{T_{w\text{con}}}$ and $T_{sat,con}$ with Q^*. As the ascending rate of $T_{sat,con}$ with Q^* at the elevated pressure was less than the increasing rate of $\overline{T_{w\text{con}}}$ for the RLT with or without coil at the FR of 0.5 or 0.8, all the Nu_{con} data in each plot of Figure 6 increased with Q^*. As an increase of Ca promoted the vapor–liquid circulation in each RLT, the Nu_{con} level was consistently raised by increasing Ca. Similarly to the comparative Nu_{eva} results between the RLTs with and without coil at the filling ratios of FR = 0.5 and 0.8, the Nu_{con} level of the RLT with coil at FR = 0.5 in Figure 5b was slightly less than that without coil in Figure 5a; whereas all the Nu_{con} values in the RLT with coil at FR = 0.8 were noticeably raised from the counterparts in the RLT without coil. Clearly, the pumping effect in the inner and outer legs of the RLT with FR = 0.8 assisted the condensation heat transfer process. The increase of FR from 0.5 to 0.8 still incurred the substantial Nu_{con} increases for both RLTs with and without coil.

Justified by the power-law-like data trends in all the plots of Figure 6, all the Nu_{con} data were correlated by Equation (16) into the function of Q^*.

$$Nu_{con} = m\{Ca\} \times Q*^{n\ \{Ca\}} \tag{16}$$

The correlative m and n coefficients for the RLTs with and without coil at FR = 0.5 and 0.8 are summarized in Table 3.

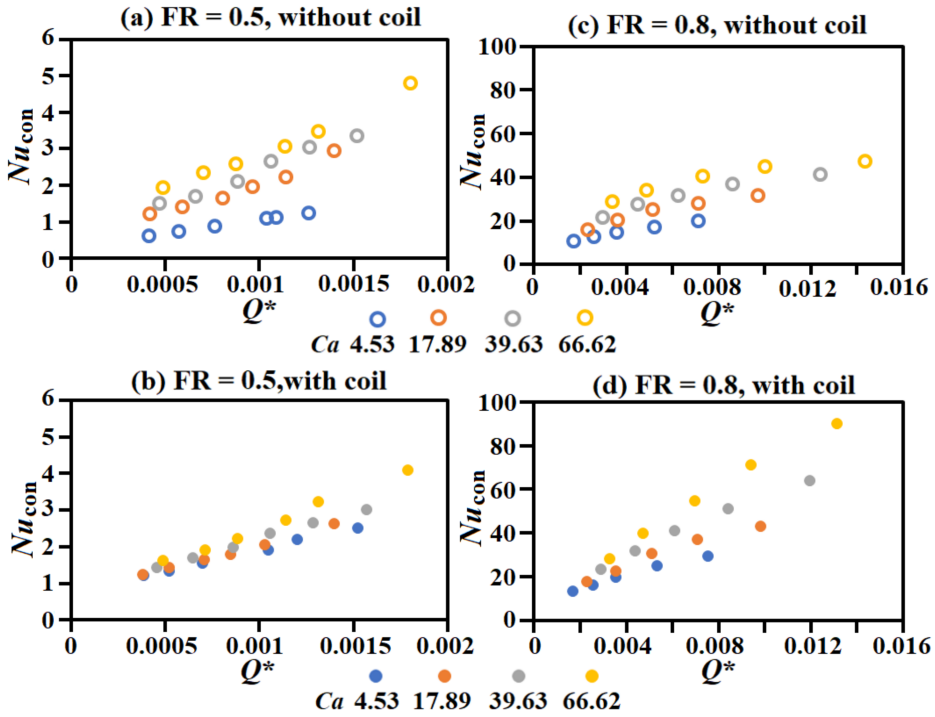


Figure 6. Nu_{con} variations against Q^* at all the *Ca* values tested for the RLTs with and without coil at the filling ratios of (**a**,**b**) 0.5 (**c**,**d**) 0.8. All the Nu_{con} data were increased with Q^* at a fixed *Ca*.

Table 3. *m* and *n* coefficients in Nu_{con} correlations for the RLTs with and without coil at FR = 0.5 and 0.8. The *m* and *n* coefficients were subsequently correlated into the functions of Ca for devising Nu_{con} correlation.

Ca	FR = 0.5				FR = 0.8			
	Without Coil		With Coil		Without Coil		With Coil	
	m	*n*	*m*	*n*	*m*	*n*	*m*	*n*
4.53	164.58	0.65	83.65	0.55	320	0.55	459.25	0.56
17.89	295.97	0.7	105.86	0.57	316.43	0.49	844.83	0.64
39.63	415.5	0.74	169.88	0.63	313.88	0.46	1598.9	0.72
66.62	502	0.77	428.53	0.74	221.84	0.35	3651.9	0.85

By plotting the coefficients *m* and *n* against *Ca*, the varying trends of *m* and *n* values followed the quadric-like variations with Ca. The combinations of *m* and *n* correlations with equation (16) generated the Nu_{con} correlations of the RLTs with and without coil at FR = 0.5 and 0.8 as Equations (17)–(20).

$$Nu_{con} = (126.73 + 9.82Ca - 0.063 - Ca^2) \times Q^{*(0.63+0.005Ca-5E-5Ca^2)}$$
Without coil at FR $= 0.5$ (17)

$$Nu_{con} = (101.88 - 2.77Ca + 0.114Ca^2) \times Q^{*(0.55+0.0007Ca+3E-5Ca^2)}$$
With coil at FR $= 0.5$ (18)

$$Nu_{con} = (306.89 + 1.98Ca - 0.048Ca^2) \times Q^{*(0.56-0.0024Ca-9E-6Ca^2)}$$
Without coil at FR $= 0.8$ (19)

$$Nu_{con} = (505.5 - 0.89Ca + 0.72Ca^2) \times Q^{*(0.55+0.0044Ca+1E-6Ca^2)}$$
With coil at FR $= 0.8$ (20)

The comparison of the Nu_{con} data with the correlative results from Equations (17) and (18) showed that the maximum discrepancy was less than ±18% for all the data generated. An examination of the functional dependencies of Nu_{eva} and Nu_{con} on Q^* in Equations (11) and (16) revealed that the ascending rate of Nu_{con} with Q^* exceeded the descending rate of Nu_{eva} with Q^*, leading to the improved K_{eff} and R_{th} performances by raising Q^*, which will be later demonstrated.

3.3. External Airflow Nusselt Numbers of Rotating Condenser Bend

To assist design applications using the RLT as a passive cooling method for the rotor of an electric motor, the heat transfer coefficient of the airflow surrounding the rotating condenser bend is required to define the thermal boundary conditions for the thermal model. Figure 7 depicts the variations of $Nu_{ext,con}$ ($h_{ext,con}$) against Re_Ω (ΩR).

As the airflows over the rotating condenser bends for all the RLTs with and without coil at the filling ratios of 0.5 and 0.8 were geometrically and dynamically similar, the four sets of $Nu_{ext,con}$ ($h_{ext,con}$) data were converged on a tight data band at each Re_Ω (ΩR) in Figure 7. Following the converged data trends in Figure 7 with a diminished airflow and, hence, forced convective heat transfer coefficient over the condenser at zero speed, the $Nu_{ext,con}$ data were well fitted by the power law function in Equation (21) with the correlative coefficient of 0.98.

$$Nu_{ext,con} = 0.089 \times {Re_\Omega}^{0.59} \quad (21)$$

3.4. Effective Thermal Conductivity of RLT

Another critical parameter for predicting the material temperatures of an electric motor with the present RLT in the rotor is the effective thermal conductivity (k_{eff}) of the RLT that varies with FR, *Ca*, and Q^*. The K_{eff} data measured from the RLTs with and without coil at FR = 0.5 and 0.8 were plotted against Q^* at a fixed *Ca* value in each plot of Figure 8, which increased consistently with Q^*. Such K_{eff} performance reflected the competing effects of Q^* on Nu_{eva} and Nu_{con}. As the increasing rate of Nu_{con} outweighed the descending rate of Nu_{eva} with Q^*, all the K_{eff} data increased with Q^* in each plot of Figure 8.

Referring to the aforementioned Q^* impacts on Nu_{eva} and Nu_{con}, the Nu_{eva} and Nu_{con} values were, respectively, decreased and increased with Q^*. Justified by the functional dependencies of Nu_{eva} and Nu_{con} on Q^* instilled in Equations (11) and (16), as illustrated previously, the rate of Nu_{con} increase with Q^* exceeded the descending rate of Nu_{eva} with Q^*, such that the consistent trend of K_{eff} increase with Q^* was resolved in Figure 8. Irrespective of the filling ratio with or without the coil insert, the effective thermal conductivity (K_{eff}, k_{eff}) was increased with Q^* by promoting the E-to-D boiling activities in each RLT prior to the dry-out limit at each *Ca* value. To respond to the improved vapor–liquid circulation and, hence, Nu_{eva} and Nu_{con} with *Ca*, as well as the differential effects of the coil in the RLTs with FR = 0.5 and 0.8, the K_{eff} data in Figure 8 for all the RLTs were increased by raising *Ca*, following the order FR = 0.8 with coil, FR = 0.8 without coil, FR = 0.5 without coil, and FR = 0.5 with coil. Similarly to the results of Nu_{eva} and Nu_{con}, the K_{eff} for the RLT with FR = 0.8 was substantially raised from that with FR = 0.5. In this regard, with the present evaporator heat flux (q_{eva}) and centrifugal acceleration in the respective ranges of 1414.93–6754.37 Wm^{-2} and 4.53–66.62 g, the K_{eff} (k_{eff}) for the RLTs at FR = 0.8 with coil, FR = 0.8 without coil, FR = 0.5 without coil, and FR = 0.5 with coil were in the ranges of 10.75–37.5 (161.19-562.43 $Wm^{-1}K^{-1}$), 9.76-26.84 (146046–402.57 $Wm^{-1}K^{-1}$), 1.02–2.48 (15.23–37.26 $Wm^{-1}K^{-1}$), and 1.04–1.87 (15.67–28 $Wm^{-1}K^{-1}$), respectively.

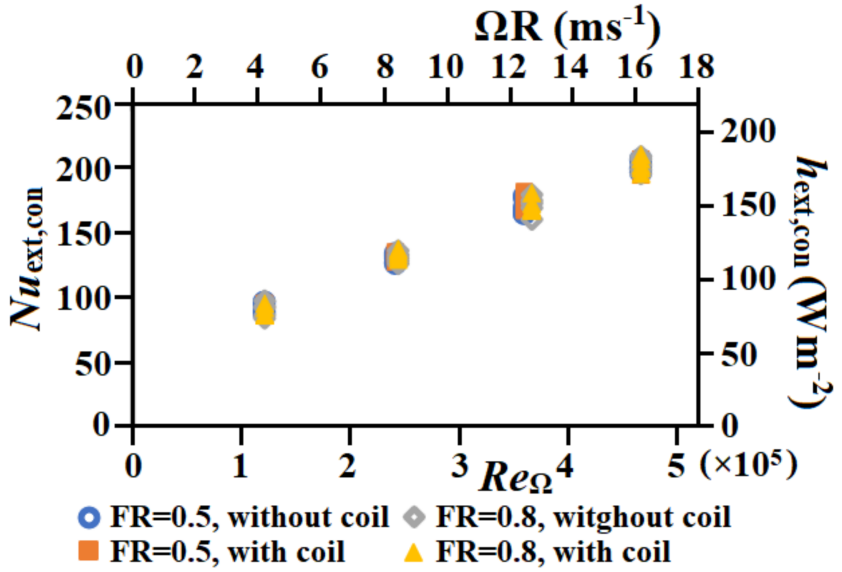


Figure 7. Variations of $Nu_{ext,con}$ ($h_{ext,con}$) against Re_{Ω} (ΩR) for all the RLTs tested. All the $Nu_{ext,con}$ data converged into a tight data trend that increased with Re_{Ω}. The devised $Nu_{ext,con}$ correlation in accordance with the converged data trend can be used to evaluate the convective heat transfer rate of the rotating condenser bend when simulating the thermal field of an electric motor with the RLTs.

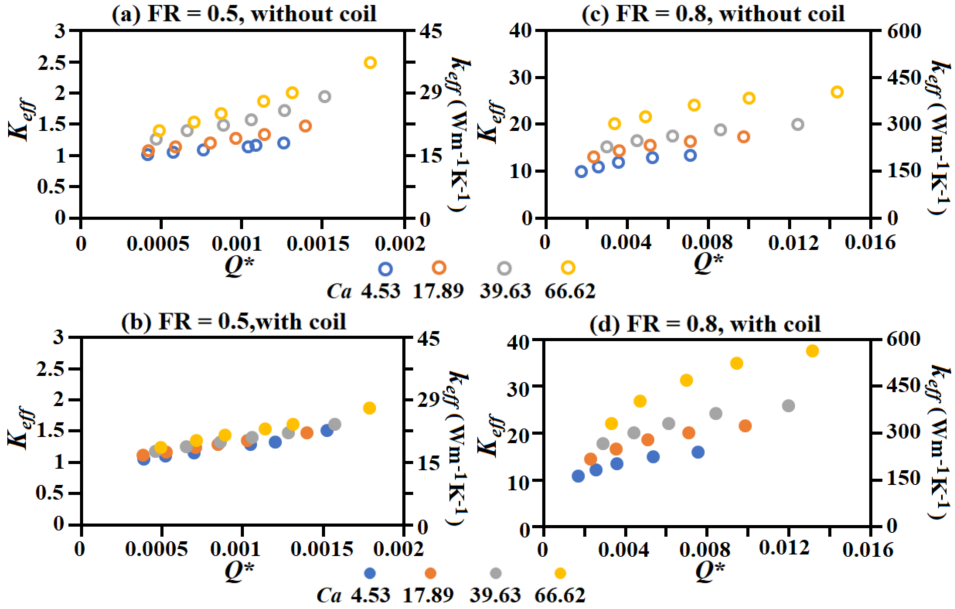


Figure 8. K_{eff} (k_{eff}) variations against Q^* at all the Ca tested for the RLTs with and without coil at the filling ratio of (**a**,**b**) 0.5 and (**c**,**d**) 0.8. All the K_{eff} (k_{eff}) data were increased with Q^* (Ca) at a fixed Ca (Q^*).

While Figure 8a,b and Figure 8c,d revealed two different patterns of data trends for the RLTs with FR = 0.5 and 0.8, irrespective as to whether the coil was present or absent, all the K_{eff} data trends in each plot of Figure 8 were converged onto unity at the limiting condition of zero Q^* to revert the conductive heat transfer along the RLT walls. For the RLTs with FR = 0.5 and 0.8, the two groups of K_{eff} data in Figure 8a,b and Figure 8c,d were well correlated by the quadratic and power law functions, respectively. In order to recover the sole conductive heat transfer scenario at $Q^* = 0$ for each RLT, the empirical K_{eff} correlations

for the RLTs with FR = 0.5 and 0.8 were, respectively, devised into Equations (22) and (23), with the limiting condition of K_{eff} = 1 at zero *Ca*.

$$K_{eff} = 1 + f\{Ca\} \times Q^* + g\{Ca\} \times Q^{*2} \quad RLTs\ with\ FR = 0.5 \tag{22}$$

$$K_{eff} = 1 + f\{Ca\} \times Q^{*g\{Ca\}} \quad RLTs\ with\ FR = 0.8 \tag{23}$$

Again, f and g values in Equations (22) and (23) were functions of Ca. When the superheated condition in the RLT with FR = 0.5 vanished by increasing FR to 0.8, the K_{eff} performances for the RLTs with and without coil were considerably modified to exhibit the higher increasing rate with Q^* than that with FR = 0.5, as characterized by Equations (22) and (23). The variations of f and g values against *Ca* for the RLTs with and without coil at FR = 0.5 and 0.8 are summarized in Table 4.

Table 4. f and g values in K_{eff} correlations for the RLTs with and without coil at FR = 0.5 and 0.8. The f and g coefficients were subsequently correlated into the functions of *Ca* for devising the K_{eff} correlation.

Ca	FR = 0.5				FR = 0.8			
	Without Coil		With Coil		Without Coil		With Coil	
	f	g	f	g	f	g	f	g
4.53	26.43	101,715	101.41	148,494	39.98	0.236	59.664	0.282
17.89	195.55	85,634	295.06	30,524	44.83	0.217	77.74	0.286
39.63	497.11	66,957	356.58	13,998	47.19	0.207	101.54	0.312
66.62	704.4	60,612	461.58	8906	62.05	0.205	194.46	0.38

The mathematic structures of the f and g functions were identified from the data trends in the plots that depicted the f and g variations with Ca. After correlating the f and g values into the functions of *Ca*, the empirical equations that evaluated K_{eff} for the RLTs with and without coil at the filling ratios of 0.5 and 0.8 are generated as Equations (24)–(27) with the maximum discrepancy between them and experimental and correlation results less than ±15% for all the data generated.

$$K_{eff} = 1 + (4.48Ca^{1.25}) \times Q^* + (140987Ca^{-0.197}) \times Q^{*2} \quad FR = 0.5\ without\ coil \tag{24}$$

$$K_{eff} = 1 + (48.18Ca^{0.56}) \times Q^* + (694443Ca^{-1.053} \times Q^{*2} \quad FR = 0.5\ with\ coil \tag{25}$$

$$K_{eff} = 1 + (41.02 - 0.0023Ca + 0.0047Ca^2) \times Q^{*(0.24-0.0014Ca+1E-5Ca^2)} \quad FR = 0.8\ without\ coil \tag{26}$$

$$K_{eff} = 1 + (64.81 - 0.385Ca + 0.035Ca^2) \times Q^{*(0.28-0.0005Ca+3E-5Ca^2)} \quad FR = 0.8\ with\ coil \tag{27}$$

3.5. Thermal Resistance of RLT

The overall thermal performances of the RLTs with and without coil at the filling ratios of 0.5 and 0.8 that responded to the combined effects of Q^* and/or *Ca* on of Nu_{eva}, Nu_{con}, and $Nu_{ext,con}$ were reflected in the various R_{th} performances shown by Figure 9, in which the variations of R_{th} (r_{th}) with Q^* at all the tested *Ca* values for the RLTs with and without coil at the filling ratios of (a,b) 0.5 and (c,d) 0.8 were compared. Following the aforementioned Q^* impacts on Nu_{eva} and Nu_{con} when the results of K_{eff} (k_{eff}) in Figure 8

were examined, as well as the consistent increases of Nu_{eva}, Nu_{con}, and $Nu_{ext,con}$ with Ca, the R_{th} (r_{th}) data in each plot of Figure 9 consistently reduced by increasing Q^* and/or Ca.

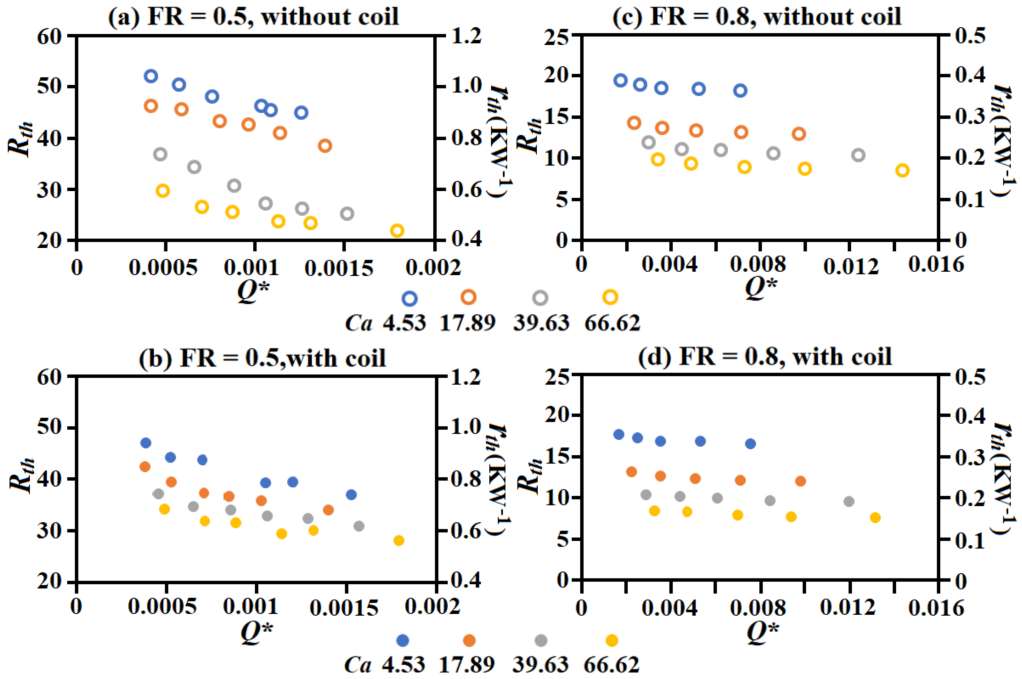


Figure 9. R_{th} (r_{th}) variations against Q^* at all the Ca values tested for the RLTs with and without coil at the filling ratios of (**a**,**b**) 0.5 and (**c**,**d**) 0.8. All the R_{th} (r_{th}) data decreased with Q^* (Ca) at a fixed Ca (Q^*).

Complying with the consistent power law decay for all the R_{th} data trends in Figure 9, the correlations of R_{th} for the RLTs took the general form of Equation (28).

$$R_{th} = i\{Ca\} \times Q^{*j\{Ca\}} \tag{28}$$

In Equation (28), the coefficient i and exponent j are both the functions of Ca. Table 5 summarizes the values of i and j for the RLTs with and without coil at FR = 0.5 and 0.8.

Table 5. i and j values in R_{th} correlations for the RLTs with and without coil at FR = 0.5 and 0.8. The i and j coefficients were subsequently correlated into the functions of Ca for devising R_{th} correlation.

Ca	FR = 0.5				FR = 0.8			
	Without Coil		With Coil		Without Coil		With Coil	
	i	*j*	*i*	*j*	*i*	*j*	*i*	*j*
4.53	17.53	−0.141	12.36	−0.17	14.47	−0.046	14.345	−0.041
17.89	15.04	−0.147	11.26	−0.168	9.32	−0.069	9.257	−0.062
39.63	8.67	−0.179	11.14	−0.157	6.85	−0.092	7.498	−0.063
66.62	5.02	−0.231	11.04	−0.149	5.61	−0.096	5.645	−0.079

The i and j variations against Ca for all the RLTs were well correlated by the quadric functions. The R_{th} correlations were obtained by substituting the i and j functions into Equation (28) for the RLTs with and without coil at FR = 0.5 and 0.8, as shown in Equations (29)–(32).

$$R_{th} = (19.3 - 0.309Ca + 0.0014Ca^2) \times Q^{*(-0.138-0.0004Ca-2E-5Ca^2)} \tag{29}$$

$$R_{th} = (12.51 - 0.067Ca + 0.0007Ca^2) \times Q^{*(-0.172-0.0003Ca+7E-7Ca^2)} \quad (30)$$

$$R_{th} = (15.62 - 0.357Ca + 0.0031Ca^2) \times Q^{*(-0.037-0.0021Ca+2E-5Ca^2)} \quad (31)$$

$$R_{th} = (15.18 - 0.312Ca + 0.0026Ca^2) \times Q^{*(-0.041-0.0008Ca+4E-6Ca^2)} \quad (32)$$

The comparison of all the R_{th} data with the results of Equations (29)–(32) revealed that the maximum discrepancy between the experimental data and the correlation results was less than ±15%. At the present experimental conditions, the R_{th} (r_{th}) for the RLTs at FR = 0.8 with coil, FR = 0.8 without coil, FR = 0.5 without coil, and FR = 0.5 with coil were in the respective ranges of 18.69–8.03 (0.36–0.16 $Wm^{-1}K^{-1}$), 19.47-8.51 (0.38–0.17 $Wm^{-1}K^{-1}$), 52.06–21.87 (0.99–0.42 $Wm^{-1}K^{-1}$), and 46.86–27.92 (0.89–0.54 $Wm^{-1}K^{-1}$). Justified by the higher K_{eff} (k_{eff}) and the lower R_{th} (r_{th}) for the RLTs at FR = 0.8 with coil in Figures 8 and 9, the rotating loop thermosyphon with the coil insert at a filling ratio of 0.8 is recommended as an effective passive cooling device in the rotor of an electric motor.

In view of practical applications, the limitations of the present test results are mainly restricted by the rotating speeds tested, giving rise to the applicable centrifugal accelerations of the RLTs in the range of 4.53–66.62 g. There were ±15–20% of discrepancies between the experimental data and the calculation results using the various empirical correlations generated. The extrapolations of the empirical correlations out of the test conditions enlarged the uncertainties from the reported maximum discrepancies between the experimental and correlative results. As the overall thermal resistance (R_{th}, r_{th}) and effective thermal conductivity (K_{eff}, k_{eff}) were measured form the average wall temperatures of evaporator and condenser, the present R_{th} and K_{eff} correlations were not suitable for predicting the localized thermal performances of the RLT.

4. Conclusions

The present study proposed the rotating loop thermosyphon (RLT) as a passive heat transfer measure for rotor cooling of an electric motor or a rotating machinery. The effects of filling ratio, Ca, and Q^* on Nu_{eva}, Nu_{con}, $Nu_{ext,con}$, K_{eff}, and R_{th} for the RLTs with and without the coil were examined to reach the following conclusion remarks.

1. The pool boiling activities in the outer leg of evaporator were, respectively, converted to the superheated and saturated film boiling processes along the inner leg of the RLTs with FR = 0.5 and 0.8. For all the RLTs tested, Nu_{eva} were decreased with Q^* but increased with Ca due to the attendant increases of evaporator pressure and $T_{sat,eva}$ with the improved vapor–liquid circulation when Ca was increased.
2. As the pressure and, hence, $T_{sat,con}$ were increased by raising Q^* and/or Ca, whereas the vapor–liquid segregation force in the condenser was amplified by increasing Ca, all the Nu_{con} data were increased with Q^* and Ca.
3. The raised airflow velocity surrounding the external surfaces of condenser by increasing Ca incurred the power-law-like $Nu_{ext,con}$ increases, regardless Q^*, FR, and the coil insert in the RLT.
4. With a liquid film in the inner leg of evaporator, by increasing FR from 0.5 to 0.8 to convert the local heating process from superheated to saturated state, all the thermal performance indexes, namely Nu_{eva}, Nu_{con}, $Nu_{ext,con}$, K_{eff}, and R_{th}, were significantly improved. The pumping effect of the coil in the inner leg of the RLT with a filling ratio of 0.8 improved the thermal performance from that without coil. In the inner leg of the RLT with a filling ratio of 0.5, the diminished liquid film prohibited the beneficial pumping effect of the coil but added vapor flow resistance to undermine the thermal performance.
5. Acting through the competing Q^* effects on Nu_{eva} and Nu_{con}, the K_{eff} (R_{th}) were increased (decreased) with Q^*. The increases of Nu_{eva} and Nu_{con} with Ca had led to the consistent increase (decrease) of K_{eff} (R_{th}) by increasing the Ca value. The K_{eff} ($1/R_{th}$) followed the order of RLT with coil at FR = 0.8, RLT without coil at FR = 0.5, RLT without coil at FR = 0.5, and RLT with coil at FR = 0.5.

6. For the RLT at FR = 0.8 with coil, the effective thermal conductivity reached the range of 161.19–562.43 $Wm^{-1}K^{-1}$ in the present test conditions, which was elevated to 107.5%–375% of the thermal conductivity of the RLT wall. The corresponding overall thermal resistances of the particular RLT fell in the range of 0.36–0.16 $Wm^{-1}K^{-1}$.
7. The empirical correlations of Nu_{eva}, Nu_{con}, $Nu_{ext,con}$, K_{eff}, and R_{th} were devised to assist the design applications for using the RLT in the rotor of an electric motor.

Author Contributions: Conceptualization, S.W.C. and P.-S.W.; methodology, S.W.C. and M.-F.H.; formal analysis, W.L.C.; investigation, S.W.C. and W.L.C.; resources, M.-F.H.; data curation, S.W.C. and W.L.C.; writing—original draft preparation, W.L.C.; writing—review and editing, S.W.C.; visualization, M.-F.H.; supervision, S.W.C., M.-F.H., and P.-S.W.; project administration, S.W.C.; funding acquisition, S.W.C. and M.-F.H. All authors have read and agreed to the published version of the manuscript.

Funding: This research was funded by the Ministry of Science and Technology, Taiwan, grant number MOST 109-2622-8-006-005.

Institutional Review Board Statement: Not applicable.

Informed Consent Statement: Not applicable.

Data Availability Statement: The data presented in this study are available on request from the corresponding author.

Conflicts of Interest: The authors declare no conflict of interest.

Nomenclature

English symbols

Ca	relative centrifugal acceleration = $\Omega^2 R/g$
d	hydraulic diameter of RLT (m)
d_c	diameter of coiled wire in RLT (m)
g	gravitational acceleration (ms^{-2})
h_{con}	heat transfer rate in condenser = $q/(T_{sat,con} - \overline{T_w}_{con})$ ($Wm^{-2}K^{-1}$)
h_{eva}	heat transfer rate in evaporator = $q/(\overline{T_w}_{eva} - T_{sat,eva})$ ($Wm^{-2}K^{-1}$)
h_{fg}	latent heat of working fluid (J/kg)
K_{eff}	non-dimensional effective thermal conductivity = k_{eff}/k_w
k_{air}	Thermal conductivity of air ($Wm^{-1}K^{-1}$)
k_{eff}	effective thermal conductivity of RLT ($Wm^{-1}K^{-1}$)
k_f	thermal conductivity of liquid water ($Wm^{-1}K^{-1}$)
k_w	thermal conductivity of RLT duct ($Wm^{-1}K^{-1}$)
k_{air}	thermal conductivity of air ($Wm^{-1}K^{-1}$)
L_{RLT}	nominal length of RLT (m)
Nu_{con}	Nusselt number in condenser of RLT = $[q/(T_{sat,con} - \overline{T_w}_{con})]d/k_f$
Nu_{eva}	Nusselt number in evaporator of RLT $[q/(\overline{T_w}_{eva} - T_{sat,eva})]d/k_f$
Q^*	dimensionless heat power = $(Qd)/(\mu_f h_{fg})$
Q	net heat power transferred by RLT (W)
R	centerline rotating radius of RLT (m)
Re_Ω	rotating Reynolds number = $\Omega R^2/\nu$
R_{th}	non-dimensional thermal resistance of RLT = $r_{th}/(k_f d)$
r_{th}	thermal resistance of RLT = $[(\overline{T_w}_{eva} - T_{amb})/Q]$
S	loop-wise coordinate (m)
T_{amb}	ambient temperature (K)
T_{sat}	saturation temperature of working fluid (K)
T_w	wall temperature of RLT (K)

Greek symbols

μ_f	dynamic viscosity of liquid water ($kgm^{-1}s^{-1}$)
ν	kinematic viscosity of the air flow (m^2s^{-1})
Ω	angular velocity of RLT (s^{-1})

Subscripts

con	condenser of RLT
eva	evaporator of RLT
ext,con	external condenser surface of RLT

Abbreviations

FR	filling ratio
RLT	rotating loop thermosyphon
RHP	rotating heat pipe

References

1. Li, S.-F.; Liu, Z. Parametric study of rotating heat pipe performance: A review. *Renew. Sustain. Energy Rev.* **2020**, *117*, 109482. [CrossRef]
2. Lee, J.S.; Kim, C.J. Heat transfer and internal flow characteristics of a coil-inserted rotating heat pipe. *Int. J. Heat Mass Transf.* **2001**, *44*, 3543–3551. [CrossRef]
3. Song, F.; Ewing, D.; Ching, C.Y. Fluid flow and heat transfer model for high-speed rotating heat pipes. *Int. J. Heat Mass Transf.* **2003**, *46*, 4393–4401. [CrossRef]
4. Song, F.; Ewing, D.; Ching, C.Y. Experimental investigation on the heat transfer characteristics of axial rotating heat pipes. *Int. J. Heat Mass Transf.* **2004**, *47*, 4721–4731. [CrossRef]
5. Song, F.; Ewing, D.; Ching, C.Y. Heat transfer in the evaporator section of moderate-speed rotating heat pipes. *Int. J. Heat Mass Transf.* **2008**, *51*, 1542–1550. [CrossRef]
6. Bertossi, R.; Guilhem, N.; Ayel, V.; Romestant, C.; Bertin, Y. Modeling of heat and mass transfer in the liquid film of rotating heat pipes. *Int. J. Therm. Sci.* **2012**, *52*, 40–49. [CrossRef]
7. Xie, M.; Xue, Z.; Qu, W.; Li, W. Experimental investigation of heat transfer performance of rotating heat pipe. *Procedia Eng.* **2015**, *99*, 746–751. [CrossRef]
8. Lian, W.; Chang, W.; Xuan, Y. Numerical investigation on flow and thermal features of a rotating heat pipe. *Appl. Therm. Eng.* **2016**, *101*, 92–100. [CrossRef]
9. Chen, J.; Fu, Y.; Gu, Z.; Shen, H.; He, Q. Study on heat transfer of a rotating heat pipe cooling system in dry abrasive-milling. *Appl. Therm. Eng.* **2017**, *115*, 736–743. [CrossRef]
10. Chatterjee, S.; Sugilal, G.; Prabhu, S.V. Flow transitions in a partially filled rotating inclined pipe with continuous flow. *Exp. Therm. Fluid Sci.* **2017**, *83*, 47–56. [CrossRef]
11. Ling, J.; Cao, Y.; Chang, W.S. Analyses of radially rotating high-temperature heat pipes for turbomachinery applications. *Trans. ASME J. Eng. Gas Turbines Power* **1999**, *121*, 306–312. [CrossRef]
12. Ling, J.; Cao, Y. Closed-form analytical solutions for radially rotating miniature high-temperature heat pipes including non-condensable gas effects. *Int. J. Heat Mass Transf.* **2000**, *43*, 3661–3671. [CrossRef]
13. Ling, J.; Cao, Y.; Lopez, A.P. Experimental investigations of radially rotating miniature high-temperature heat pipes. *Trans. ASME J. Heat Transf.* **2001**, *123*, 113–119. [CrossRef]
14. Waowaew, N.; Terdtoon, P.; Maezawa, S.; Kamonpet, P.; Klongpanich, W. Correlation to predict heat transfer characteristics of a radially rotating heat pipe at vertical position. *Appl. Therm. Eng.* **2003**, *23*, 1019–1032. [CrossRef]
15. Aboutalebi, M.; Moghaddam, A.M.N.; Mohammadi, N.; Shafii, M.B. Experimental investigation on performance of a rotating closed loop pulsating heat pipe. *Int. Commun. Heat Mass Transf.* **2013**, *45*, 137–145. [CrossRef]
16. Li, Y.; Li, Z.; Chen, C.; Yan, Y.; Zeng, Z.; Li, B. Thermal responses of heat pipes with different wick structures under variable centrifugal accelerations. *Appl. Therm. Eng.* **2016**, *96*, 352–363. [CrossRef]
17. Chen, J.; Fu, Y.; He, Q.; Shen, H.; Ching, C.Y.; Ewing, D. Environmentally friendly machining with a revolving heat pipe grinding wheel. *Appl. Therm. Eng.* **2016**, *107*, 719–727. [CrossRef]
18. Chang, S.W.; Cai, W.L. Thermal performance of two-phase thermosyphon loop in rotating thin pad. *Int. J. Therm. Sci.* **2017**, *112*, 270–288. [CrossRef]
19. On-ai, K.; Kammuang-lue, N.; Terdtoon, P.; Sakulchangsatjatai, P. Implied physical phenomena of rotating closed-loop pulsating heat pipe from working fluid temperature. *Appl. Therm. Eng.* **2019**, *148*, 1303–1309. [CrossRef]
20. Liou, T.-M.; Chang, S.W.; Cai, W.L.; Lan, I.-A. Thermal fluid characteristics of pulsating heat pipe in radially rotating thin pad. *Int. J. Heat Mass Transf.* **2019**, *131*, 273–290. [CrossRef]
21. Faghri, A.; Gogineni, S.; Thomas, S. Vapor flow analysis of an axially rotating heat pipe. *Int. J. Heat Mass Transf.* **1993**, *36*, 2293–2303. [CrossRef]
22. Jankowski, T.A.; Prenger, F.C.; Razani, A. Experimental study of a curved rotating heat pipe. *Trans. ASME J. Heat Transf.* **2008**, *130*, 101601. [CrossRef]
23. Yau, Y.H.; Foo, Y.C. Comparative study on evaporator heat transfer characteristics of revolving heat pipes filled with R134a, R22 and R410A. *Int. Commun. Heat Mass Transf.* **2011**, *38*, 202–211. [CrossRef]
24. Hassan, H.; Harmand, S. An experimental work on the effect of the radius of rotation on the performance of revolving heat pipe (RVHP). *Appl. Therm. Eng.* **2017**, *123*, 537–545. [CrossRef]

25. Gundabattini, E.; Mystkowski, A.; Idzkowski, A.; Singh, R.; Solomon, D.G. Thermal mapping of a high-speed electric motor used for traction applications and analysis of various cooling methods-a review. *Energies* **2021**, *14*, 1472. [CrossRef]
26. Deisenroth, D.C.; Ohadi, M. Thermal management of high-power density electric motors for electrification of aviation and beyond. *Energies* **2019**, *12*, 3594. [CrossRef]
27. Canders, W.-R.; Hoffmann, J.; Henke, M. Cooling technologies for high power density electrical machines for aviation applications. *Energies* **2019**, *12*, 4579. [CrossRef]
28. Guo, F.; Zhang, C. Oil-cooling method of the permanent magnet synchronous motor for electric vehicle. *Energies* **2019**, *12*, 2984. [CrossRef]
29. Fujita, H.; Itoh, A.; Urano, T. Newly developed motor cooling method using refrigerant. *World Electr. Veh.* **2019**, *10*, 38. [CrossRef]
30. Wu, P.-S.; Hsieh, M.-F.; Cai, W.L.; Liu, J.-H.; Huang, Y.-T.; Caceres, J.F.; Chang, S.W. Heat transfer and thermal management of interior permanent magnet synchronous electric motor. *Inventions* **2019**, *4*, 69. [CrossRef]
31. Kline, S.J.; McClintock, F.A. Describing uncertainties in single sample experiments. *Mech. Eng.* **1953**, *75*, 3–8.